Article

Symmetry Analysis of Magnetoelectric Effects in Perovskite-Based Multiferroics

Zukhra Gareeva [1,2,*] **, Anatoly Zvezdin** [3]**, Konstantin Zvezdin** [3] **and Xiangming Chen** [4]

1   Institute of Molecule and Crystal Physics, Subdivision of the Ufa Federal Research Centre of the Russian Academy of Sciences, Prospect Octyabrya 151, 450075 Ufa, Russia

2   Institute of Physics and Technology, Bashkir State University, ul. Z. Validi 32, 450076 Ufa, Russia

3   Prokhorov General Physics Institute of the Russian Academy of Sciences, ul. Vavilova 38, 119991 Moscow, Russia; zvezdin.ak@phystech.edu (A.Z.); zvezdin.ka@phystech.edu (K.Z.)

4   Laboratory of Dielectric Materials, School of Materials Science and Engineering, Zhejiang University, Zheda Road 38, Hangzhou 310027, China; xmchen59@zju.edu.cn

*   Correspondence: zukhragzv@yandex.ru; Tel.: +7-(917)-8049560

Abstract: In this article, we performed symmetry analysis of perovskite-based multiferroics: bismuth ferrite ($BiFeO_3$)-like, orthochromites ($RCrO_3$), and Ruddlesden–Popper perovskites ($Ca_3Mn_2O_7$-like), being the typical representatives of multiferroics of the trigonal, orthorhombic, and tetragonal crystal families, and we explored the effect of crystallographic distortions on magnetoelectric properties. We determined the principal order parameters for each of the considered structures and obtained their invariant combinations consistent with the particular symmetry. This approach allowed us to analyze the features of the magnetoelectric effect observed during structural phase transitions in $Bi_xR_{1-x}FeO_3$ compounds and to show that the rare-earth sublattice has an impact on the linear magnetoelectric effect allowed by the symmetry of the new structure. It was shown that the magnetoelectric properties of orthochromites are attributed to the couplings between the magnetic and electric dipole moments arising near Cr^{3+} ions due to distortions linked with rotations and deformations of the CrO_6 octahedra. For the first time, such a symmetry consideration was implemented in the analysis of the Ruddlesden–Popper structures, which demonstrates the possibility of realizing the magnetoelectric effect in the Ruddlesden–Popper phases containing magnetically active cations, and allows the estimation of the conditions required for its optimization.

Keywords: keyword multiferroics; crystal lattices; symmetry; perovskites; magnetoelectric effect

1. Introduction

Multiferroic, multifunctional materials attract enormous research activity due to the prospects of their implementation in science and technology. The collective state parameters attainable in multiferroics (MFs) are preferable for advanced spintronic devices based on the use of combinatorial functions due to their high efficiency, low power consumption, and adaptability [1].

Despite the variety of currently known magnetoelectric materials, perovskite-like structures remain the most researched MFs compounds. The family of perovskites stands out for its diversity due to the intrinsic instability of the cubic parent perovskite phase [2]. Crystallographic distortions owing to the substitution of various cations at A and B positions can lead to the emergence of ferroelectric and MF properties due to the hybridization of ion orbitals, tilt of oxygen octahedra (BO_6), doping of various cations, and other factors [3]. ABO_3 perovskites can produce a variety of MFs differing in the type of (i) ferroelectric ordering (A- or B-driven ferroelectricity), as in the cases of $EuTiO_3$ [4] and $BiFeO_3$ [5]; (ii) magnetic ordering (although most perovskite MFs are G-type antiferromagnets (AFM), canted ferromagnetism and a combination of ferromagnetic and AFM phases are also possible) [6,7]; (iii) mechanism of magnetoelectric coupling, which can be associated with

magnetoelectrically active d-ions or f-ions ($RFeO_3$) [8], the Dzyaloshinskii–Moriya interaction ($BiFeO_3$) [5], spin–orbit coupling (BiMnTe) [9], antiferroelectric orderings ($RCrO_3$)) [10]; and (iv) temperatures of ferroelectric and magnetic orderings, which remain low enough for most perovskite-based MFs.

Quite recently, the MF community turned to hybrid layered perovskite structures, considering them as prospective candidates for high-temperature MFs. We refer to layered structures composed of an n-layered perovskite with a single-layer spacer in-between. Depending on the kind of single-layer spacer, one can distinguish the Ruddlesden–Popper (RP) $A'_2(A_{n-1}B_nO_{3n+1})$, Dion–Jacobson (DJ) $A'(A_{n-1}B_nO_{3n+1})$, and Aurivillius $Bi_2O_2(A_{n-1}B_nO_{3n+1})$ structures [11,12]. When n = ∞, the layered perovskite transforms into a classical perovskite.

Among layered perovskites, the most widespread and studied compounds are the RP structures. They received their name in honor of the chemists R. Ruddlesden and P. Popper, who, in 1957, synthesized the series of Sr_2TiO_4, $Sr_3Ti_2O_7$, and $Sr_4Ti_3O_{10}$ phases, forming a class of complex oxides $Sr_{n+1}Ti_nO_{3n+1}$ [13]. Since then, the class of RP structures has expanded significantly, and, at present, it includes various compounds with the general formula $A'_2(A_{n-1}B_nO_{3n+1})$, where A' = La, Sr, Li, . . . ; A = Sr, Ca, K, . . . ; and B = Ti, Fe, Mn, Nb, ... The advantages of RP-type perovskites are related to long-term chemical stability, the activity of oxygen reduction reaction, and the possibility of realizing nontrivial magnetic and electrical properties [11–17]. Due to the activity of the reaction with oxygen, RP structures find applications in solid oxide fuel cells [14]. As for magnetoelectricity, interest in layered perovskites is associated with the discoveries of the colossal magnetoresistance effect in the early 2000s in RP structures with magnetoactive cations ($Ca_3Mn_2O_7$, . . .) [14–19] and ferroelectricity at room temperatures, found in $Ca_{3-x}Sr_xTi_2O_7$ in 2015 [20] and then in $Sr_3M_2O_7$-based oxides and other RP phases [21]. Currently, RP structures are considered promising candidates for high-temperature MFs. The crystal structure, instabilities, and structural phase transitions occurring in RP oxides are well known; however, a number of questions concerning ferroelectricity, magnetic ordering, and their coupling is open for discussion.

The focus of this manuscript was the study of the magnetoelectric effect in $Bi_{1-x}R_xFeO_3$, $RCrO_3$, and $Ca_3(Ti_{1-x}Mn_x)_2O_7$ multiferroics (MFs). We aimed to develop a unified approach to the analysis of the perovskite-like multiferroics based on the symmetry of the material, taking crystallographic distortions as the primary order parameters.

It is valuable to note that the classification of distortions and the search for recipes for effective magnetoelectric couplings in MFs with a perovskite structure is a long-standing and, at the same time, 'hot' problem. We refer to several reviews, references therein, and original papers that discussed various classification schemes for perovskite distortions and group-theoretical approaches, including their implementation in online tools (in particular, ones on the Bilbao Crystallographic Server) for identification of active order parameters, and their possible couplings and invariant polynomials [22–29]. However, distortion classification schemes mainly deal with BO6 octahedrons and do not account for polar distortions, which have significant impact on ferroelectric and MF properties; in addition, they also have limitations for specific systems. Despite the power of the software tools, they have not yet been applied to each MF system; for example, the details of the magnetoelectric coupling in MFs with a variable concentration of rare-earth ions have not yet been investigated, and the same statement is also applied to the RP structures.

Thus, in our research, we appealed to group-theoretical analysis, which is an elegant and effective tool for studying the properties of crystals with a complex magnetic structure, to classify the distortive, ferroelectric, and magnetic orderings in several classes of perovskite MFs. For this purpose, we examined typical MF structures with the perovskite parent phase: $BiFeO_3$, $RCrO_3$, $Ca_3Mn_2O_7$, in which small distortions in the crystallographic lattice lead to systems of different symmetry (trigonal, orthorhombic, and tetragonal). Using the methods of theoretical group analysis, we considered how the symmetry manifests itself in their magnetoelectric properties. We determined magnetic and structural modes,

classified them according to the irreducible representations of the corresponding symmetry group, and calculated the coefficients of magnetoelectric couplings.

2. Materials and Methods

In this section, we analyze the crystal structure, and ferroelectric and magnetic properties of representatives of the perovskite-based multiferroics and, using the methods of the theoretical group analysis, determine the features of their magnetoelectric properties.

2.1. Multiferroic BiFeO$_3$

We start our consideration with the well-known multiferroic BiFeO$_3$ with high temperatures of ferroelectric and magnetic orderings (T$_C$ = 1083 K, T$_N$ = 643 K). BiFeO$_3$ crystallizes in the nonpolar symmetry group *R3c* and is a ferroelectric material. The high-symmetry perovskite group is reduced to *R3c* due to three types of distortions: (i) relative displacement of Bi and Fe ions along <111> axis, (ii) deformations of oxygen octahedrons, and (iii) counterrotation of oxygen octahedrons around Fe ions. The displacements of Bi and Fe ions from their centrosymmetric positions lead to spontaneous electric polarization P_s directed along one of the <111> crystallographic axes [30]. The magnitude of polarization has been the subject of controversy for a while. As was reported in Refs. [5,20,31–35], spontaneous polarization in the BiFeO$_3$ crystal and films can attain values varying from 6 to 150 μC/cm^2. Electric polarization is sufficiently low, P_s~6–9 μC/cm^2, in single crystals and ceramic samples [34,35]; the large values of P_s, around 100 μC/cm^2, are achieved under epitaxial strain in the films [5,36–38]; and they can also be related to the supertetragonal phase induced by the strain.

The rigorous estimation of electronic polarization requires the implementation of quantum mechanics, including electronic structure methods with correspondence to experimentally measurable observables [39]. In the frame of these approaches in Ref. [40], electric polarization in perovskite BiFeO$_3$ was calculated as a function of percentage distortion from the high-symmetry nonpolar structure to the ground-state *R3c* structure, which gives the value 95.0 μC cm^{-2}. However, as was shown in Ref. [30], similar results can be obtained with the use of the point charge model, where the electric polarization is represented through the atomic displacements of Bi^{3+} and O^{2-} ions.

$$P = \frac{4e}{V}(3\zeta_R - 4\zeta_{O1} - 2\zeta_{O3}) \tag{1}$$

where *e* is the elementary charge, *V* is the unit cell volume, ζ_R is the displacement of Bi ions corresponding to (i) distortion, and ζ_{O1} and ζ_{O3} are the displacements of oxygen ions corresponding to (ii)—distortion.

In magnetic relation, BiFeO$_3$ is weak ferromagnet with G-type antiferromagnetic (AFM) ordering characterized by AFM vector $\boldsymbol{L} = \frac{1}{V}\sum_{i=1}^{6}(-1)^i \boldsymbol{\mu}_i$, where $\boldsymbol{\mu}_i$ are the magnetic moments of six Fe ions in a unit cell. The canting of spins is related to rotations of oxygen octahedrons FeO6, determined by the vector $\boldsymbol{\Omega}$, the distortions of (iii)—type [41], which have an impact on the weak ferromagnetic vector, determined as

$$\boldsymbol{M} = \frac{V_0 a^2}{6J}\boldsymbol{\Omega} \times \boldsymbol{L} + \frac{V_0 a^2}{6J}\sum_{n=1}^{6}(\boldsymbol{n}_n \times \zeta_{O_n}) \tag{2}$$

where V_0 is a constant, *a* is the lattice parameter, *J* is the exchange constant, and $\boldsymbol{n}_n$ is the direction vector, oriented along one of the <100> crystallographic axes. Here, we used an assumption that the Heisenberg exchange constant remains unchanged, which is a commonly used approximation for multiferroic BiFeO$_3$; in particular, the deviation (noncollinearity) of the nearest-neighbor spins is accounted for by the antisymmetric Dzyaloshinskii–Moriya exchange interaction [42,43]. AFM spin arrangement is superimposed with a spatially modulated magnetic structure with a large period λ = (620 ± 20 Å) incommensurate with

the lattice parameter [44]. The magnetic moments of Fe ions retain their local mutually antiferromagnetic G-type orientation and rotate along the propagation direction of the modulation in the plane perpendicular to the basal crystal plane.

To explore the magnetoelectric effect (MEE) in $BiFeO_3$, we appealed to symmetry analysis. Knowledge of crystal structure and symmetry is of primary importance for this approach. To consider the properties of $BiFeO_3$, the space group $R3\bar{c}$ was taken as a 'parent' symmetry phase [45]. $R3\bar{c}$ differs from the space symmetry group $R3c$ of $BiFeO_3$ single crystals only by the presence of a polar vector $\boldsymbol{P} = (0, 0, P_s)$. The symmetry analysis of the magnetoelectric properties of $BiFeO_3$ has been performed in Refs. [45–47]. Here, we focused our attention on the magnetoelectric tensor α_{ij}, which links the electric polarization and the magnetic field

$$P_i = \alpha_{ij} H_j \tag{3}$$

As was shown in Ref. [47] for $BiFeO_3$ crystals, the tensor α_{ij} can be expressed through the components of the AFM vector $\boldsymbol{L}$

$$\alpha_{ij}^{BiFeO_3} = \begin{vmatrix} -a_1 L_x & a_4 L_z + a_1 L_y & a_2 L_y \\ a_1 L_y - a_4 L_z & a_1 L_x & -a_2 L_x \\ -a_3 L_y & a_3 L_x & 0 \end{vmatrix} \tag{4}$$

As seen from Equations (3) and (4), the symmetry allows the linear magnetoelectric effect; however, due to the presence of an incommensurate space-modulated structure, it is not observed in $BiFeO_3$. Thus, when the spin cycloidal structure is destroyed, the linear magnetoelectric effect is restored. It can be achieved by applying a strong magnetic field, pressure, or doping $BiFeO_3$ with rare-earth ions. In recent years, a series of experimental studies has been conducted, indicating the enhancement of the magnetoelectric effect in $BiFeO_3$ multilayers and composites.

Here, we discuss the replacement of various rare-earth (RE) ions at the A-positions as a way to improve the MF properties of $BiFeO_3$, a route that was paved in the 1990s [30,45–50], and current research confirms its efficiency [6,51]. As was shown in Ref. [51], La-substitution in $Bi_{1-x}La_xFeO_3$ (x = 0.08~0.22) ceramics induces a continuous structural evolution from $R3c$ to $Pna2_1$ and, finally, the $Pbnm$ phase. To understand the properties of $Bi_{1-x}R_xFeO_3$ structures (R = La, Gd, Dy, . . .), it is reasonable to introduce the AFM vector ($\boldsymbol{l}$), which characterizes the magnetic ordering of the rare-earth sublattice, and to consider the $Pbnm$ space symmetry group as the parent phase in the $Bi_{1-x}R_xFeO_3$ structure, keeping in mind structural phase transitions $Pbnm \rightarrow Pna2_1$. The space group $Pbnm$ contains eight irreducible representations, where their matrix representations are given in the columns corresponding to the generating symmetry elements (Table 1). The vector components of magnetic field $\boldsymbol{H}$, electric polarization $\boldsymbol{P}$, magnetization $\boldsymbol{M}$, and antiferromagnetic vectors $\boldsymbol{L}$ and $\boldsymbol{l}$ form the irreducible representations and are placed in the last column in Table 1 according to their transformation properties. Table 1 allows the determination of the transformation properties of AFM vector components, exchange-coupled structures, and magnetoelectric invariants, contributing to the magnetoelectric energy of the $Bi_{1-x}R_xFeO_3$ structure.

$$\Phi_{me}^{B_{1-x}R_xFeO_3} = P_z\big(\gamma_1(l_zM_y - l_yM_z) + \gamma_2(l_xL_y - l_yL_x)\big) + P_x\big(\gamma_{xyx}(l_yM_x - l_xM_y) + \gamma_2(l_yL_z - l_zL_y)\big) + \\ P_y\Big(\gamma_3 l_xM_x + \gamma_2 l_xL_z + \gamma_4\big(l_yM_y + L_y^2\big)\Big) \tag{5}$$

where γ_i are the magnetoelectric coefficients,

$$\gamma_1 = \gamma_{zzy}, \gamma_2 = \gamma_{xyz}, \gamma_3 = \gamma_{yxx}, \gamma_4 = \gamma_{yyy}$$

Table 1. Irreducible representations of the *Pbnm* symmetry group.

Γ_i	$\bar{1}$	2_x	2_y	2_z	Order Parameters, and Magnetic and Electric Fields		
Γ_1	1	1	1	1	L_y		
Γ_2	1	1	-1	-1	M_x	L_z	H_x
Γ_3	1	-1	1	-1	M_y		H_y
Γ_4	1	-1	-1	1	M_z	L_x	H_z
Γ_5	-1	1	1	1	l_y		
Γ_6	-1	1	-1	-1	l_x	P_z	E_z
Γ_7	-1	-1	1	-1		P_y	E_y
Γ_8	-1	-1	-1	1	l_z	P_x	E_x

The magnetoelectric coupling coefficient for the $Bi_{1-x}R_xFeO_3$ structures can be determined as follows

$$\alpha_{ij} = \begin{vmatrix} a_1(l_xL_x + l_zL_z) & a_{12}l_x & -a_{13}l_y \\ a_{12}l_z & a_2l_y & a_{23}l_x \\ a_{13}l_y & a_{32}l_z & a_1(l_xL_x + l_zL_z) \end{vmatrix} \approx \begin{vmatrix} 0 & a_{12}l_x & -a_{13}l_y \\ a_{12}l_z & a_2l_y & a_{23}l_x \\ a_{13}l_y & a_{32}l_z & 0 \end{vmatrix} \quad (6)$$

In the case of $Bi_{1-x}R_xFeO_3$, rare-earth elements can have a significant impact on magnetoelectric properties. As seen from Equation (6), α_{ij} depends on the components of the AFM vector of the rare-earth sublattice (for the case of nonzero magnetization on the R ion site), and it is possible to distinguish a linear MEE related to rare-earth elements, and a quadratic MEE emerges due to cross-coupling of the AFM vectors of iron and rare-earth sublattices.

2.2. Magnetoelectric Properties of RCrO₃

In this section, we consider MEE in the rare-earth orthochromites ($RCrO_3$), focusing on the relation of magnetoelectric properties with crystallographic distortions. The crystal structure of $RCrO_3$ belongs to the space symmetry group *Pbnm/Pnma* [52–54]. Its orthorombically distorted perovskite unit cell contains 4 $RCrO_3$ molecules (Figure 1). In addition, 4 Cr^{3+} and 4 R^{3+} magnetic ions (in the case of R = rare-earth ion) are located in the local positions differing by the symmetry of O^{2-} environments. The *d*-ions (M^{3+}) occupy the position 4*b*, the *f*-ions (R^{3+}) occupy the position 4*c*, and oxygen ions occupy the positions 4*c* and 8*d* (in Wyckoff notation).
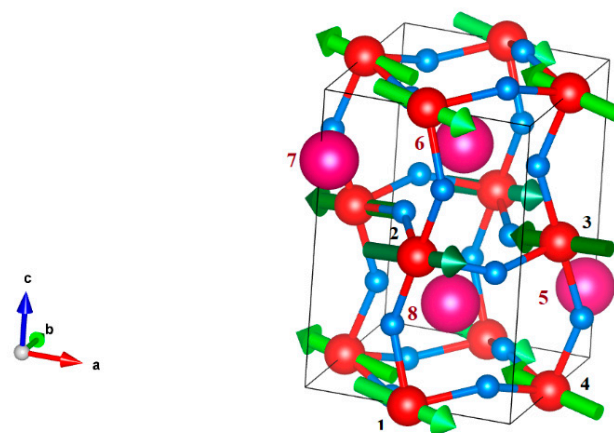

Figure 1. Electric dipole moments arrangement in $RCrO_3$ unit cell, a, b, c are the principal crystal axes, Cr ions are numbered as 1, 2, 3, 4; R ions are numbered as 5, 6, 7, 8. Green arrows denote the orientation of electric dipole moments in the vicinity of Cr^{3+} ions ordered by antiferroelectric **D** mode.

Magnetic moments of the *d*-ions determined by the vectors M_i (i = 1–4) constitute 4 transition metal magnetic sublattices, and the magnetic moments of the *f*-ions determined by vectors m_i (i = 1–4) constitute 4 rare-earth magnetic sublattices. The combinations between magnetic moments of the *d*- and the *f*-sublattices determine magnetic modes of the '*d*' ions:

$$F = M_1 + M_2 + M_3 + M_4, \; A = M_1 - M_2 - M_3 + M_4$$

$$G = M_1 - M_2 + M_3 - M_4, C = M_1 + M_2 - M_3 - M_4 \tag{7}$$

and magnetic modes of the '*f*'- ions:

$$f = m_1 + m_2 + m_3 + m_4, \; a = m_1 - m_2 - m_3 + m_4,$$
$$g = m_1 - m_2 + m_3 - m_4, \; c = m_1 + m_2 - m_3 - m_4 \tag{8}$$

Neutron diffraction measurements showed that RCrO$_3$ exhibits one of three *G*-type AFM configurations with weak magnetic components $\Gamma_1 (A_x, G_y, C_z)$, Γ_2 (F_x, C_y, G_z), and Γ_4 ($G_x A_y F_z$).

In contrast to BiFeO$_3$, the ferroelectric properties of RCrO$_3$ are weak, and the Curie ordering temperatures are low (T$_C$~130–250 K) [55,56]. However, as recent experiments have shown, during the polishing of samples in an electric field, an electric polarization of the order of 0.06 µC/cm^2 is induced; moreover, the electric field affects the spin–reorientation phase transitions, which indicates the presence of magnetoelectric coupling in the material [57,58].

As expected, the magnetoelectric behavior is owed to the crystallographic distortions, which are quite different from those in BiFeO$_3$. In the case of RCrO$_3$, the principal distortions are related to the antirotation of the CrO6 octahedrons around the [110] direction and the displacements of R ions from A-positions in the perovskite parent phase. Octahedron rotation is described by the axial vectors ω_i (i = 1 ÷ 4) linked to Cr ions, and, as was shown in Ref. [10], they contribute to the axial order parameter.

$$\Omega_b = \omega_1 - \omega_2 + \omega_3 - \omega_4 \tag{9}$$

Polar order parameters related to the displacements of oxygen and rare-earth ions are also allowed. To compose the polar order parameters, we consider the electric dipole moments $d_i = qr_i$ emerging in the vicinity of the Cr ions, where $r_q = \sum_i q_i r_{qi} / \sum_i q_i$ is the position of the electric dipole charge center, q_i are the signed magnitudes of the charges, and r_{qi} are the radius vectors of the charges in the local reference frame. For the perovskite-like compounds,

$$r_q = \frac{\left(+\frac{3}{8}e\right) \cdot \sum\limits_{i=1}^{8} r_R + \left(-\frac{2}{2}e\right) \cdot \sum\limits_{i=1}^{6} r_O}{\left|8 \cdot \left(+\frac{3}{8}e\right) + 6 \cdot \left(-\frac{2}{2}e\right)\right|} \quad r = (x, y, z) \tag{10}$$

where *e* is the elementary charge, r_R are the radius vectors of the rare-earth ions, and r_O are the radius vectors of the oxygen ions measured from the Cr^{3+} ion.

As in the case of magnetic moments (7), (8), electric dipoles $d_i = qr_i$ constitute 4 ferroelectric sublattices, and the combinations between dipole moments determine ferroelectric modes reads.

$$P = d_1 + d_2 + d_3 + d_4$$
$$Q_2 = d_1 - d_2 - d_3 + d_4$$
$$Q_3 = d_1 - d_2 + d_3 - d_4 \tag{11}$$
$$D = d_1 + d_2 - d_3 - d_4$$

The arrangement of the dipole moments in RCrO$_3$ is shown in Figure 1; as can be seen, they form an antiferroelectric structure ordered according to the *D*-mode. Direct calculation of the dipole moments shows that the value of *D* is maximum, and the values of *P*, $Q_{2,3}$ are negligible.

The transformation properties of the order parameters introduced above can be found using the irreducible representations of the space symmetry group of the RCrO$_3$ compounds given in Table 2.

Table 2. Irreducible representations of the *Pnma* symmetry group.

Γ_i	$\bar{1}$	2_x	2_y	2_z	Magnetic OPs, Magnetic Field		Structural OPs, Electric Field
						4b	4c
Γ_1	1	1	1	1	A_z, G_x, C_y	c_y	Ω_{bx}
Γ_2	1	1	-1	-1	F_z, G_y, C_x, H_z	f_z, c_x	Ω_{by}
Γ_3	1	-1	1	-1	F_x, A_y, C_z, H_x	f_x, c_z	
Γ_4	1	-1	-1	1	F_y, A_x, G_z, H_y	f_y	Ω_{bz}
Γ_5	-1	1	1	1		g_z, a_x	Q_{2z}, Q_{3x}, D_z
Γ_6	-1	1	-1	-1		a_y	P_z, E_z, Q_{3y}
Γ_7	-1	-1	1	-1		a_z, g_x	P_y, Q_{2x}, E_y, D_x
Γ_8	-1	-1	-1	1		g_y	P_x, Q_{2y}, E_x, D_y

Knowledge of their transformation properties makes it possible to understand how crystallographic distortions manifest themselves in magnetic and ferroelectric orderings. As in the previous subsection, classification of the components of order parameters according to the irreducible representations of the *Pnma* symmetry group allows us to determine exchange-coupled magnetic structures, the possible electrostatically coupled dipole structures, to compose the invariant combination of order parameters contributing to the thermodynamic potential and to calculate the magnetoelectric coupling coefficient.

$$P_x = (\alpha_{xyx}a_y + \alpha_{xzyx}g_zG_yG_x + \alpha_{xxyx}a_xG_yG_x)H_x + (\alpha_{xxy}a_x + \alpha_{xxyy}f_xG_yG_x + \alpha_{xzyy}c_zG_yG_x + \alpha_{xzy}g_z)H_y + \ldots$$

$$F_x = (\alpha^*_{xyx}a_y + \alpha^*_{xzyx}g_zG_yG_x + \alpha^*_{xxyx}a_xG_yG_x)E_x + (\alpha^*_{xxy}a_x + \alpha^*_{xxyy}f_xG_yG_x + \alpha^*_{xzyy}c_zG_yG_x + \alpha^*_{xzy}g_z)E_y + \ldots \quad (12)$$

The magnetoelectric coefficient in terms of the components of G and g vectors is written as follows.

$$\alpha_{ij}^{RCrO_3} = \begin{vmatrix} a_1 G_x\left(g_zG_y - g_yG_z\right) & a_2 g_z & a_3 g_x \\ a_2 g_z & a_1 G_x\left(g_zG_y - g_yG_z\right) & a_4 g_y \\ a_4 g_y & a_3 g_x & a_2 g_z \end{vmatrix} \quad (13)$$

At the end of this section, we draw the reader's attention to the fact that the presented analysis applies to rare-earth orthoferrites RFeO$_3$. RFeO$_3$ compounds crystallize in the same space symmetry group *Pnma*, and several of these crystals exhibit nonlinear magnetoelectric responses [23,25,59]. The magnetoelectric tensor (12) can also be used to describe their magnetoelectric properties.

2.3. Ruddlesden–Popper Structures

Ruddlesden–Popper (RP) structures are attracting considerable attention due to the recently discovered high-temperature ferroelectric properties and the prospects for their potential implementation as multiferroics at room temperature [11]. The presence of ferroelectric properties, the so-called hybrid improper ferroelectricity (HIF), was theoretically predicted in double-layered perovskite compounds Ca$_3$Mn$_2$O$_7$ and Ca$_3$Ti$_2$O$_7$, and then detected experimentally in Ca$_{3-x}$Sr$_x$Ti$_2$O$_7$ single crystals [20], and in Ca$_3$(Ti$_{1-x}$Mn$_x$)$_2$O$_7$ ceramics [21].

In this section, we plan to focus on the RP manganite phases Ca$_3$(Ti$_{1-x}$Mn$_x$)$_2$O$_7$ as they contain magnetic Mn ions and, as shown in Ref. [21], are room-temperature HIF materials. In the limiting case x = 1, Ca$_3$(Ti$_{1-x}$Mn$_x$)$_2$O$_7$ transforms into the RP phase Ca$_3$Mn$_2$O$_7$,

which was thoroughly explored due to the colossal magnetoresistance effect found in the $(CaO)\text{-}(CaMnO_3)_n$ (n =1, 2, 3, ∞) RP structures in the 2000s [16–19]. The structures with n = 1 (2D-structure) and n = ∞ (perovskite) are considered as the end members of the RP series, so the double-layered RP structures receive more attention.

The temperature of AFM ordering T_N = 115 K in $Ca_3Mn_2O_7$ was first experimentally found in Ref. [16], where it was assumed that there is a G-type AFM order. A neutron diffraction study [19] revealed the dominant contribution of the G-type or C-type AFM phase with an AFM spin arrangement within the bi-layer plane. In that work, the possibility of the existence of a weak ferromagnetic (WFM) state in the RP phase $Ca_3Mn_2O_7$ was also assumed. A further study on $Ca_3Mn_2O_7$ showed the transition to the AFM state at the temperature T_N = 134 K and a signature of WFM below 100 K [60,61].

The crystal structure, structural phase transitions, and polar phases of $Ca_3Ti_2O_7$ [62] and $Ca_3Mn_2O_7$ [19,63] with double-layered RP structures, studied since 1998 [16], have now been proven [21]. Above room temperature (RT), the crystal structure of $Ca_3Mn_2O_7$ is described by the tetragonal space group *I4/mmm*, and at RT, by the space group $Cmc2_1$ [64]. The transition from the *I4/mmm* to $Cmc2_1$ phase should occur through an intermediate phase, which can be either *Cmcm* or *Cmca*, as follows from the first-principles calculations [46]. The transition into the ferroelectric phase is observed close to T_C = 280 K, at which the transition into the $Cmc2_1$ phase occurs. As experimental measurements indicate that ferroelectric ordering in $Ca_3Mn_2O_7$ occurs up to RT, the existence of an intermediate ferroelectric state is expected here.

Structural transformations can arise due to the substitution of magnetic ions at the A-positions $(Ca_{3-x}La_xMn_2O_7)$ or ferroelectric ions in the B-positions $(Ca_3(Ti_{1-x}Mn_x)_2O_7)$. The tetragonal-to-orthorhombic transition presumable through the phases *I4/mmm* $\rightarrow$ *Fmmm* $\rightarrow$ *Cmcm* $\rightarrow$ $Cmc2_1$, occurring in the 200–300 °C range, was observed during the study of $Ca_{3-x}La_xMn_2O_7$ structures [19,64]. Though the existence of *I4/mmm* and $Cmc2_1$ phases is confirmed, the presence of 'intermediate' phases is still under discussion.

Thus, in further consideration, we can take the tetragonal *I4/mmm* structure $(Ca_3Mn_2O_7)$ as the parent phase and apply the symmetry analysis, employed in the previous sections, to explore the magnetoelectric properties of the RP structures. According to the data of the synchrotron X-ray diffraction study [19], the Mn ions occupy the 4e positions (in the Wyckoff notation) in the *I4/mmm* phase, which indicates the presence of 4 magnetic sublattices μ_i (i = 1÷4) with magnetic moments of the same magnitude. Possible combinations of the vectors μ_i give us the basic magnetic vectors.

$$\begin{aligned}
\boldsymbol{F} &= \boldsymbol{\mu}_1 + \boldsymbol{\mu}_2 + \boldsymbol{\mu}_3 + \boldsymbol{\mu}_4 \\
\boldsymbol{A} &= \boldsymbol{\mu}_1 - \boldsymbol{\mu}_2 - \boldsymbol{\mu}_3 + \boldsymbol{\mu}_4 \\
\boldsymbol{G} &= \boldsymbol{\mu}_1 - \boldsymbol{\mu}_2 + \boldsymbol{\mu}_3 - \boldsymbol{\mu}_4 \\
\boldsymbol{C} &= \boldsymbol{\mu}_1 + \boldsymbol{\mu}_2 - \boldsymbol{\mu}_3 - \boldsymbol{\mu}_4
\end{aligned} \tag{14}$$

The unit cell of $Ca_3Mn_2O_7$ shown in Figure 2 contains 2 formula units $Ca_3Mn_2O_7$. The positions of the symmetry elements I, C_2^z, C_4^z, C_2^y (generators of *I4/mmm* space group) in the unit cell are depicted in Figure 2b in accordance with Figure 2a. Note that the local symmetry elements of the 4e{4mm} positions, which are the 4_z axis (principal crystal axis) and 4 planes of symmetry *m* passing through this axis, remain even for magnetic ions, occupying the 4e positions.

In accordance with Figure 2, it is easy to compose permutation transformations of the ions at the 4e positions (Table 3) and permutation transformations of basis vectors (Table 4).
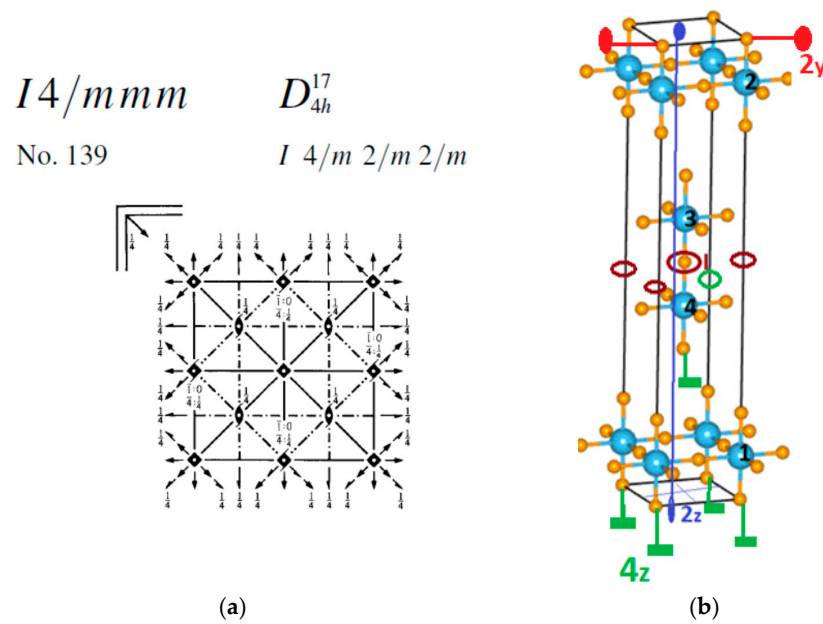
	(a)		(b)

Figure 2. (**a**) $I4/mmm$ space symmetry group elements; (**b**) $Ca_3Mn_2O_7$ unit cell, the numbering of magnetic ions is presented, the arrangement of the symmetry elements is also shown-the axes of symmetry $4_z, 2_z, 2_y$ and the centers of inversion I.

Table 3. Permutation transformations ions in positions 4e {4mm}.

G_F	1	2	3	4
$\bar{1}$	2	1	4	3
4_z	1	2	3	4
2_z	3	4	1	2
2_y	2	1	4	3

Table 4. Permutation transformations of basis vectors.

G_F	F	A	G	C
$\bar{1}$	F	$-A$	$-G$	C
4_z	F	A	G	C
2_z	F	$-A$	G	$-C$
2_y	F	$-A$	$-G$	C

Using Table 4, we obtain a cipher (Turov indices) for AFM vectors, which explains how the symmetry elements transform magnetic sublattices into each other.

$$A: 4_z(+)2_z^1(-)2_y(-)\bar{1}(-)$$

$$G: 4_z(+)2_z^1(+)2_y(-)\bar{1}(-)$$

$$C: 4_z(+)2_z^1(-)2_y(+)\bar{1}(+)$$

In consistence with the data of experimental studies [16,19], we assume the G-type of AFM ordering. In this case, the values of AFM vectors *A* and *C* are taken to be sufficiently small and we can restrict our consideration with two magnetic order parameters instead of 4. Thus, we leave the ferromagnetic vector *M* = *F* and the antiferromagnetic vector *L* = *G* as the basic magnetic parameters. Then, we classify them together with the polarization vector according to the irreducible representation of the space symmetry group D_{4h}^{17} (Table 5). The

first line of Table 5 contains generators of the D_{4h}^{17} group $G = \left\{ E, I, C_2^y, C_2^z, C_4^{z+} \right\}$, where the last column contains basic magnetic and ferroelectric functions.

Table 5. Irreducible representations of the $I4/mmm$ symmetry group and basic functions.

Γ_i	E	$2C_{4z}$	C_{2z}	$2C_{2y}$	$\bar{1}$	Basic Vectors *F*, *G*, *P*
Γ_1	1	1	1	1	1	
Γ_2	1	1	1	-1	1	F_z
Γ_3	1	-1	1	-1	1	
Γ_4	1	-1	1	1	1	
Γ_5	$\begin{pmatrix} 1 & 0 \\ 0 & 1 \end{pmatrix}$	$\begin{pmatrix} 0 & 1 \\ -1 & 0 \end{pmatrix}$	$\begin{pmatrix} -1 & 0 \\ 0 & -1 \end{pmatrix}$	$\begin{pmatrix} -1 & 0 \\ 0 & 1 \end{pmatrix}$	$\begin{pmatrix} 1 & 0 \\ 0 & 1 \end{pmatrix}$	$\begin{pmatrix} F_x \\ F_y \end{pmatrix}$
Γ_6	1	1	1	1	-1	G_z
Γ_7	1	1	1	-1	-1	P_z
Γ_8	1	-1	1	-1	-1	
Γ_9	1	-1	1	1	-1	
Γ_{10}	$\begin{pmatrix} 1 & 0 \\ 0 & 1 \end{pmatrix}$	$\begin{pmatrix} 0 & 1 \\ -1 & 0 \end{pmatrix}$	$\begin{pmatrix} -1 & 0 \\ 0 & -1 \end{pmatrix}$	$\begin{pmatrix} -1 & 0 \\ 0 & 1 \end{pmatrix}$	$\begin{pmatrix} -1 & 0 \\ 0 & -1 \end{pmatrix}$	$\begin{pmatrix} P_x \\ P_y \end{pmatrix}$
Γ'_{10}	$\begin{pmatrix} 1 & 0 \\ 0 & 1 \end{pmatrix}$	$\begin{pmatrix} 0 & 1 \\ -1 & 0 \end{pmatrix}$	$\begin{pmatrix} -1 & 0 \\ 0 & -1 \end{pmatrix}$	$\begin{pmatrix} 1 & 0 \\ 0 & -1 \end{pmatrix}$	$\begin{pmatrix} -1 & 0 \\ 0 & -1 \end{pmatrix}$	$\begin{pmatrix} G_x \\ G_y \end{pmatrix}$

The decomposition of the basic functions into irreducible representations of the symmetry group $I4/mmm$ allows one to obtain information on the properties of a system. It is seen that the ferromagnetic and antiferromagnetic vectors transform according to the different IRs. In this case the transformation of *F* and *L* into each other can occur due to external factors, such as the electric field or strain. The combinations $F_z(P_xG_x + P_yG_y), G_z(F_xP_x + F_yP_y), P_z(F_xG_x + F_yP_zG_y), F_zP_zG_z$, transforming on Γ_1, are invariants and have an impact on magnetoelectric energy.

$$\Phi_{me} = \gamma_2 F_z(P_xG_x + P_yG_y) + \gamma_3 G_z(F_xP_x + F_yP_y) + \gamma_4 P_z(F_xG_x + F_yG_y) + \gamma_5 F_zP_zG_z \quad (15)$$

where

$$\gamma_2 = \gamma_{zxx} = \gamma_{zyy}, \gamma_3 = \gamma_{xxz} = \gamma_{yyz}, \gamma_4 = \gamma_{xzx} = \gamma_{yzy}, \gamma_5 = \gamma_{zzz}$$

Using Table 5 we calculate the magnetoelectric coupling tensor.

$$\alpha_{ij}^{R-P} = \begin{vmatrix} \gamma_3 G_z & 0 & \gamma_2 G_x \\ 0 & \gamma_3 G_z & \gamma_2 G_y \\ \gamma_4 G_x & \gamma_4 G_y & \gamma_5 G_z \end{vmatrix} \quad (16)$$

As seen from Equation (16) it linearly depends on the components of antiferromagnetic vector *G*. This finding allows us to conclude that the linear magnetoelectric effect is allowed by the symmetry of the RP structures.

3. Results and Conclusions

To summarize, we applied symmetry analysis to the magnetic and magnetoelectric properties of multiferroics (MFs) with a perovskite structure. One of the reasons for choosing perovskite-based MFs as the object of this study is related to the structural instability of the initial perovskite phase, which can lead to a variety of structures with different symmetry. This allows us to demonstrate how crystallographic distortions of various types, even if they are small enough, significantly alter the magnetic and ferroelectric orderings and their couplings. As the typical examples, we considered (i) the family of high-temperature multiferroics $Bi_xR_{1-x}FeO_3$ recognizable by their magnetoelectric proper-

ties; (ii) the rare-earth orthochromites $RCrO_3$, promising candidates for MFs, compounds with well-known magnetic structures; and (iii) the RP structures containing magnetic cations, such as $Ca_3(Ti_{1-x}Mn_x)_2O_7$, novel high-temperature MFs, the ferroelectric and magnetic properties of which are still being researched. These structures crystallize into trigonal, orthorhombic, and tetragonal syngonies, respectively, which allows us to trace the relationship between magnetoelectric properties and the symmetry of a structure, and to consider impacts given by crystallographic distortions.

The direct contribution of the distortion into electric polarization and weak ferromagnetism was considered, using $BiFeO_3$ as an example. We also analyzed the influence of structural transformation of the $Bi_xR_{1-x}FeO_3$ family on their magnetoelectric properties. Calculations showed that the linear magnetoelectric effect, suppressed by the spin-modulated structure in pure $BiFeO_3$, becomes allowed due to the symmetry of the new phase in $Bi_xR_{1-x}FeO_3$, where it is attributed mainly to rare earth (R) ions.

In the case of the rare-earth orthochromites $RCrO_3$, it was shown that the ferroelectric and magnetoelectric properties are due to crystallographic distortions. The displacements of oxygen ions from their positions in the initial perovskite phase results in the emergence of electric dipole moments in the vicinity of the Cr ions, which are coupled with the magnetic moments of the Cr ions. The distortive, ferroelectric, and magnetic order parameters were classified according to irreducible representations of the *Pnma* symmetry group of $RCrO_3$, which allows the invariant combinations to be composed between these parameters.

For the first time, a similar symmetry consideration was implemented in the analysis of the Ruddlesden–Popper structures. Taking into account the local symmetry of magnetic ions in the RP unit cell, we introduced the relevant magnetic order parameters and classified them according to the irreducible representation of the *I4/mmm* symmetry group, which describes the tetragonal symmetry of the RP structures. Analysis exemplified on the $Ca_3(Ti_{1-x}Mn_x)_2O_7$ compounds demonstrated the possibility of realizing MEE in the RP phases containing magnetically active cations and allowed the estimation of the magnetoelectric contribution to the thermodynamic potential.

In conclusion, this research allowed us to compare the magnetoelectric effects for different crystal systems of perovskites and thus design a more meaningful organization of the desired experiments.

Institutional Review Board Statement: Not applicable.

Informed Consent Statement: Not applicable.

References

1. Manipatruni, S.; Nikonov, D.E.; Lin, C.-C.; Gosavi, T.A.; Liu, H.; Prasad, B.; Huang, Y.-L.; Bonturim, E.; Ramesh, R.; Young, I.A. Scalable Energy-Efficient Magnetoelectric Spin–Orbit Logic. *Nature* **2019**, *565*, 35–42. [CrossRef]
2. Dubrovin, R.M.; Alyabyeva, L.N.; Siverin, N.V.; Gorshunov, B.P.; Novikova, N.N.; Boldyrev, K.N.; Pisarev, R.V. Incipient multiferroicity in Pnma fluoroperovskite NaMnF$_3$. *Phys. Rev. B* **2020**, *101*, 180403. [CrossRef]
3. Liu, H.; Yang, X. A brief review on perovskite multiferroics. *Ferroelectrics* **2017**, *507*, 69–85. [CrossRef]
4. Ke, X.; Birol, T.; Misra, R.; Lee, J.-H.; Kirby, B.; Schlom, D.G.; Fennie, C.J.; Freeland, J.W. Structural control of magnetic anisotropy in a strain-driven multiferroic EuTiO$_3$ thin film. *Phys. Rev. B* **2013**, *88*, 094434. [CrossRef]
5. Catalan, G.; Scott, J.F. Physics and Applications of Bismuth Ferrite. *Adv. Mater.* **2009**, *21*, 2463–2485. [CrossRef]

6. Lin, P.-T.; Li, X.; Zhang, L.; Yin, J.-H.; Cheng, X.-W.; Wang, Z.-H.; Wu, Y.-C.; Wu, G.-H. La-doped BiFeO$_3$: Synthesis and multiferroic property study. *Chin. Phys. B* **2014**, *23*, 047701. [CrossRef]

7. Savosta, M.M.; Novák, P.; Maryško, M.; Jirák, Z.; Hejtmánek, J.; Englich, J.; Kohout, J.; Martin, C.; Raveau, B. Coexistence of antiferromagnetism and ferromagnetism in Ca1−xPrxMnO3 (x<~0.1)manganites. *Phys. Rev. B* **2000**, *62*, 9532–9537. [CrossRef]

8. Zvezdin, A.K.; Mukhin, A.A. Magnetoelectric interactions and phase transitions in a new class of multiferroics with improper electric polarization. *JETP Lett.* **2008**, *88*, 505–510. [CrossRef]

9. Shikin, A.M.; Estyunin, D.A.; Zaitsev, N.L.; Glazkova, D.; Klimovskikh, I.I.; Filnov, S.O.; Rybkin, A.G.; Schwier, E.F.; Kumar, S.; Kimura, A.; et al. Sample-dependent Dirac-point gap in MnBi2Te4 and its response to applied surface charge: A combined photoemission and ab initio study. *Phys. Rev. B* **2021**, *104*, 115168. [CrossRef]

10. Zvezdin, A.K.; Gareeva, Z.V.; Chen, X.M. Multiferroic Order Parameters in Rhombic Antiferromagnets RCrO$_3$. *J. Phys. Condens. Matter* **2021**, *33*, 385801. [CrossRef]

11. Zhang, B.H.; Liu, X.Q.; Chen, X.M. Review of experimental progress of hybrid improper ferroelectricity in layered perovskite oxides. *J. Phys. D Appl. Phys.* **2021**, *55*, 113001. [CrossRef]

12. Evans, H.A.; Mao, L.; Seshadri, R.; Cheetham, A.K. Layered Double Perovskites. *Annu. Rev. Mater. Sci.* **2021**, *51*, 351–380. [CrossRef]

13. Ruddlesden, S.N.; Popper, P. The compound Sr$_3$Ti$_2$O$_7$ and its structure. *Acta Crystallogr.* **1958**, *11*, 54–55. [CrossRef]

14. Ding, P.; Li, W.; Zhao, H.; Wu, C.; Zhao, L.; Dong, B.; Wang, S. Review on Ruddlesden–Popper perovskites as cathode for solid oxide fuel cells. *J. Phys. Mater.* **2021**, *4*, 022002. [CrossRef]

15. Saw, A.K.; Gupta, S.; Dayal, V. Structural, magneto transport and magnetic properties of Ruddlesden–Popper La$_{2-2x}$Sr$_{1+2x}$Mn$_2$O$_7$ ($0.42 \leq x \leq 0.52$) layered manganites. *AIP Adv.* **2021**, *11*, 025331. [CrossRef]

16. Battle, P.D.; Rosseinsky, M.J. Synthesis, structure, and magnetic properties of n = 2 Ruddlesden–Popper manganates. *Curr. Opin. Solid State Mater. Sci.* **1999**, *4*, 163–170. [CrossRef]

17. Fawcett, I.D.; Sunstrom; Greenblatt, M.; Croft, M.; Ramanujachary, K.V. Structure, Magnetism, and Properties of Ruddlesden−Popper Calcium Manganates Prepared from Citrate Gels. *Chem. Mater.* **1998**, *10*, 3643–3651. [CrossRef]

18. Harris, A.B. Symmetry analysis for the Ruddlesden-Popper systems Ca$_3$Mn$_2$O$_7$ and Ca$_3$Ti$_2$O$_7$. *Phys. Rev. B* **2011**, *84*, 064116. [CrossRef]

19. Lobanov, M.; Greenblatt, M.; Caspi, E.A.N.; Jorgensen, J.D.; Sheptyakov, D.; Toby, B.; Botez, C.E.; Stephens, P.W. Crystal and magnetic structure of the Ca$_3$Mn$_2$O$_7$ Ruddlesden–Popper phase: Neutron and synchrotron x-ray diffraction study. *J. Phys. Condens. Matter* **2004**, *16*, 5339–5348. [CrossRef]

20. Oh, Y.S.; Luo, X.; Huang, F.-T.; Wang, Y.; Cheong, S.-W. Experimental demonstration of hybrid improper ferroelectricity and the presence of abundant charged walls in (Ca,Sr)$_3$Ti$_2$O$_7$ crystals. *Nat. Mater.* **2015**, *14*, 407–413. [CrossRef] [PubMed]

21. Liu, X.Q.; Wu, J.W.; Shi, X.X.; Zhao, H.J.; Zhou, H.Y.; Qiu, R.H.; Zhang, W.Q.; Chen, X.M. Hybrid improper ferroelectricity in Ruddlesden-Popper Ca$_3$(Ti,Mn)$_2$O$_7$ ceramics. *Appl. Phys. Lett.* **2015**, *106*, 202903. [CrossRef]

22. Glazer, A.M. The classification of tilted octahedra in perovskites. *Acta Crystallogr. Sect. B Struct. Crystallogr. Cryst. Chem.* **1972**, *28*, 3384–3392. [CrossRef]

23. Senn, M.S.; Bristowe, N. A group-theoretical approach to enumerating magnetoelectric and multiferroic couplings in perovskites. *Acta Crystallogr. Sect. A Found. Adv.* **2018**, *74*, 308–321. [CrossRef] [PubMed]

24. Mulder, A.T.; Benedek, N.A.; Rondinelli, J.M.; Fennie, C.J. Turning ABO3Antiferroelectrics into Ferroelectrics: Design Rules for Practical Rotation-Driven Ferroelectricity in Double Perovskites and A$_3$B$_2$O$_7$ Ruddlesden-Popper Compounds. *Adv. Funct. Mater.* **2013**, *23*, 4810–4820. [CrossRef]

25. Bousquet, E.; Cano, A. Non-collinear magnetism in multiferroic perovskites. *J. Phys. Condens. Matter* **2016**, *28*, 123001. [CrossRef] [PubMed]

26. Narayanan, N.; Graham, P.J.; Rovillain, P.; O'Brien, J.; Bertinshaw, J.; Yick, S.; Hester, J.; Maljuk, A.; Souptel, D.; Büchner, B.; et al. Reduced Crystal Symmetry as Origin of the Ferroelectric Polarization within the Incommensurate Magnetic Phase of TbMn$_2$O$_5$. *arXiv* **2021**, arXiv:2109.05164.

27. Mato, J.M.P.; Ribeiro, J.L.; Petricek, V.; Aroyo, M.I. Magnetic superspace groups and symmetry constraints in incommensurate magnetic phases. *J. Phys. Condens. Matter* **2012**, *24*, 163201. [CrossRef]

28. Hatch, D.M.; Stokes, H.T. INVARIANTS: Program for obtaining a list of invariant polynomials of the order-parameter components associated with irreducible representations of a space group. *J. Appl. Crystallogr.* **2003**, *36*, 951–952. [CrossRef]

29. (International Tables for Crystallography) Introduction to the Properties of Tensors. Available online: https://onlinelibrary.wiley.com/iucr/itc/Da/ch1o1v0001/ (accessed on 27 December 2021).

30. Gabbasova, Z.; Kuz'min, M.; Zvezdin, A.; Dubenko, I.; Murashov, V.; Rakov, D.; Krynetsky, I. Bi$_{1-x}$R$_x$FeO$_3$ (R = rare earth): A family of novel magnetoelectrics. *Phys. Lett. A* **1991**, *158*, 491–498. [CrossRef]

31. Palkar, V.R.; John, J.; Pinto, R. Observation of saturated polarization and dielectric anomaly in magnetoelectric BiFeO$_3$ thin films. *Appl. Phys. Lett.* **2002**, *80*, 1628–1630. [CrossRef]

32. Lebeugle, D.; Colson, D.; Forget, A.; Viret, M.; Bonville, P.; Marucco, J.F.; Fusil, S. Room-temperature coexistence of large electric polarization and magnetic order in BiFeO$_3$ single crystals. *Phys. Rev. B* **2007**, *76*, 024116. [CrossRef]

33. Lebeugle, D.; Colson, D.; Forget, A.; Viret, M. Very large spontaneous electric polarization in BiFeO$_3$ single crystals at room temperature and its evolution under cycling fields. *Appl. Phys. Lett.* **2007**, *91*, 022907. [CrossRef]

34. Teague, J.R.; Gerson, R.; James, W. Dielectric hysteresis in single crystal BiFeO₃. *Solid State Commun.* **1970**, *8*, 1073–1074. [CrossRef]
35. Wang, Y.P.; Yuan, G.L.; Chen, X.Y.; Liu, J.-M.; Liu, Z.G. Electrical and magnetic properties of single-phased and highly resistive ferroelectromagnet BiFeO₃ ceramic. *J. Phys. D: Appl. Phys.* **2006**, *39*, 2019–2023. [CrossRef]
36. Li, J.; Wang, J.; Wuttig, M.; Ramesh, R.; Wang, N.; Ruette, B.; Pyatakov, A.P.; Zvezdin, A.K.; Viehland, D. Dramatically enhanced polarization in (001), (101), and (111) BiFeO₃ thin films due to epitiaxial-induced transitions. *Appl. Phys. Lett.* **2004**, *84*, 5261–5263. [CrossRef]
37. Dixit, H.; Beekman, C.; Schlepütz, C.M.; Siemons, W.; Yang, Y.; Senabulya, N.; Clarke, R.; Chi, M.; Christen, H.M.; Cooper, V.R. Understanding Strain-Induced Phase Transformations in BiFeO₃ Thin Films. *Adv. Sci.* **2015**, *2*, 1500041. [CrossRef] [PubMed]
38. Sando, D.; Agbelele, A.; Rahmedov, D.; Liu, J.; Rovillain, P.; Toulouse, C.; Infante, I.; Pyatakov, A.P.; Fusil, S.; Jacquet, E.; et al. Crafting the magnonic and spintronic response of BiFeO₃ films by epitaxial strain. *Nat. Mater.* **2013**, *12*, 641–646. [CrossRef]
39. Resta, R.; Vanderbilt, D. Theory of Polarization: A Modern Approach. In *Physics of Ferroelectrics: A Modern Perspective; Topics in Applied Physics*; Springer: Berlin/Heidelberg, Germany, 2007; pp. 31–68. [CrossRef]
40. Spaldin, N.A. A beginner's guide to the modern theory of polarization. *J. Solid State Chem.* **2012**, *195*, 2–10. [CrossRef]
41. Gareeva, Z.; Diéguez, O.; Iñiguez, J.; Zvezdin, A.K. Complex domain walls in BiFeO₃. *Phys. Rev. B* **2015**, *91*, 060404. [CrossRef]
42. Zvezdin, A.K.; Pyatakov, A.P. On the Problem of Coexistence of the Weak Ferromagnetism and the Spin Flexoelectricity in Multiferroic Bismuth Ferrite. *EPL Europhys. Lett.* **2012**, *99*, 57003. [CrossRef]
43. Fishman, R.S.; Rõõm, T.; de Sousa, R. Normal modes of a spin cycloid or helix. *Phys. Rev. B* **2019**, *99*, 064414. [CrossRef]
44. Sosnowska, I.; Neumaier, T.P.; Steichele, E. Spiral magnetic ordering in bismuth ferrite. *J. Phys. C Solid State Phys.* **1982**, *15*, 4835–4846. [CrossRef]
45. Kadomtseva, A.M.; Zvezdin, A.K.; Popov, Y.F.; Pyatakov, A.P.; Vorob'Ev, G.P. Space-time parity violation and magnetoelectric interactions in antiferromagnets. *JETP Lett.* **2004**, *79*, 571–581. [CrossRef]
46. Kadomtseva, A.M.; Popov, Y.F.; Pyatakov, A.P.; Vorob'Ev, G.P.; Zvezdin, A.K.; Viehland, D. Phase transitions in multiferroic BiFeO3crystals, thin-layers, and ceramics: Enduring potential for a single phase, room-temperature magnetoelectric 'holy grail'. *Phase Transitions* **2006**, *79*, 1019–1042. [CrossRef]
47. Popov, Y.F.; Kadomtseva, A.M.; Vorob'Ev, G.P.; Zvezdin, A.K. Discovery of the linear magnetoelectric effect in magnetic ferroelectric BiFeO₃ in a strong magnetic field. *Ferroelectrics* **1994**, *162*, 135–140. [CrossRef]
48. Pyatakov, A.P.; Zvezdin, A.K. Magnetoelectric and multiferroic media. *Phys.-Uspekhi* **2012**, *55*, 557–581. [CrossRef]
49. Murashov, V.A.; Rakov, D.N.; Ehkonomov, N.A. Quadratic Magnetoelectric Effect in Monocrystalline (Bi,La)FeO₃. *Fiz. Tverd. Tela* **1990**, *32*, 2156–2158.
50. Sosnowska, I.; Przeniosło, R.; Fischer, P.; Murashov, V. Neutron diffraction studies of the crystal and magnetic structures of BiFeO₃ and Bi₀.₉₃La₀.₀₇FeO₃. *J. Magn. Magn. Mater.* **1996**, *160*, 384–385. [CrossRef]
51. Chen, J.; Liu, L.; Zhu, X.L.; Gareeva, Z.V.; Zvezdin, A.K.; Chen, X.M. The involvement of Pna21 phase in the multiferroic characteristics of La/Lu co-substituted BiFeO₃ ceramics. *Appl. Phys. Lett.* **2021**, *119*, 112901. [CrossRef]
52. Belov, K.P.; Zvezdin, A.K.; Kadomtseva, A.M.; Levitin, R.Z. Spin-reorientation transitions in rare-earth magnets. *Sov. Phys. Uspekhi* **1976**, *19*, 574. [CrossRef]
53. Turov, E.A. Can the magnetoelectric effect coexist with weak piezomagnetism and ferromagnetism? *Phys.-Uspekhi* **1994**, *37*, 303–310. [CrossRef]
54. Izyumov, Y.A.; Naish, V.E. Symmetry Analysis in Neutron Diffraction Studies of Magnetic Structures: 1. A Phase Transition Concept to Describe Magnetic Structures in Crystals. *J. Magn. Magn. Mater.* **1979**, *12*, 239–248. [CrossRef]
55. Tassel, C.; Goto, Y.; Kuno, Y.; Hester, J.; Green, M.; Kobayashi, Y.; Kageyama, H. Direct Synthesis of Chromium Perovskite Oxyhydride with a High Magnetic-Transition Temperature. *Angew. Chem.* **2014**, *126*, 10545–10548. [CrossRef]
56. Singh, K.D.; Singh, F.; Choudhary, R.J.; Kumar, R. Consequences of R3+ Cationic Radii on the Dielectric and Magnetic Behavior of RCrO₃ Perovskites. *Appl. Phys. A* **2020**, *126*, 148. [CrossRef]
57. Sanina, V.A.; Khannanov, B.K.; Golovenchits, E.I.; Shcheglov, M.P. Electric Polarization in ErCrO3 Induced by Restricted Polar Domains. *Phys. Solid State* **2019**, *61*, 370–378. [CrossRef]
58. Rajeswaran, B.; Khomskii, D.I.; Zvezdin, A.K.; Rao, C.N.R.; Sundaresan, A. Field-Induced Polar Order at the N\'eel Temperature of Chromium in Rare-Earth Orthochromites: Interplay of Rare-Earth and Cr Magnetism. *Phys. Rev. B* **2012**, *86*, 214409. [CrossRef]
59. Tokunaga, Y.; Furukawa, N.; Sakai, H.; Taguchi, Y.; Arima, T.; Tokura, Y. Composite Domain Walls in a Multiferroic Perovskite Ferrite. *Nat. Mater.* **2009**, *8*, 558–562. [CrossRef]
60. Sahlot, P.; Jana, A.; Awasthi, A.M. Exchange Bias in Multiferroic Ca₃Mn₂O₇ Effected by Dzyaloshinskii-Moriya Interaction. *AIP Conf. Proc.* **2018**, *1942*, 130009. [CrossRef]
61. Jung, W.-H. Weak Ferromagnetism of n = 2 Ruddlesden: Popper Ca₃Mn₂O₇ System. *J. Mater. Sci. Lett.* **2000**, *19*, 2037–2038. [CrossRef]
62. Elcombe, M.M.; Kisi, E.H.; Hawkins, K.D.; White, T.J.; Goodman, P.; Matheson, S. Structure Determinations for Ca₃Ti₂O₇, Ca₄Ti₃O₁₀, Ca₃.₆Sr₀.₄Ti₃O₁₀ and a Refinement of Sr₃Ti₂O₇. *Acta Crystallogr. B* **1991**, *47*, 305–314. [CrossRef]
63. Guiblin, N.; Grebille, D.; Leligny, H.; Martin, C. Ca₃Mn₂O₇. *Acta Crystallogr. C* **2002**, *58*, i3–i5. [CrossRef] [PubMed]
64. Bendersky, L.A.; Chen, R.; Fawcett, I.D.; Greenblatt, M. TEM Study of the Electron-Doped Layered La₂₋₂ₓCa₁₊₂ₓMn₂O₇: Orthorhombic Phase in the 0.8. *J. Solid State Chem.* **2001**, *157*, 309–323. [CrossRef]